Accepted by Nature Materials 10/31/07

Mechanical Annealing and Source-limited Deformation in Submicron-diameter Ni Crystals

Z. W. Shan[1,2], Raj Mishra[3], S.A. Syed Asif[2], Oden L. Warren[2], and Andrew M. Minor[1*]

[1]*National Center for Electron Microscopy, Lawrence Berkeley National Laboratory, Berkeley, California 94720, USA*

[2]*Hysitron Incorporated, 10025 Valley View Road, Minneapolis, Minnesota 55344, USA*

[3]*General Motors Research and Development Center, Warren, Michigan 48090, USA*

The fundamental processes that govern plasticity and determine strength in crystalline materials at small length scales have been studied for over fifty years[1-3]. Recent studies of single crystal metallic pillars with diameters of a few tens of microns or less have clearly demonstrated that the strengths of these pillars increase as their diameters decrease[4-7], leading to new models and simulations of this dramatic size effect[8-17]. Through *in situ* nanocompression experiments inside a transmission electron microscope we can directly observe the deformation of these pillar structures and correlate the measured stress values with discrete plastic events. Our experiments show that submicron nickel crystals microfabricated into pillar structures contain a high density of initial defects after processing but can be made dislocation-free by applying purely mechanical stress. This phenomenon, termed "mechanical annealing", leads to clear evidence of source-limited deformation where atypical hardening occurs through the progressive activation and exhaustion of dislocation sources.

In 1952 Herring and Galt[3] reported that the measured tensile strength of Sn whiskers (filamentary crystals a few microns in diameter and a few millimeters in length) may approach the theoretical value for a perfect Sn lattice. Thereafter, the relationship between the size of crystalline materials and their mechanical properties has been the subject of numerous experimental studies[2, 18] and scientific debates[1, 8, 9,]. The general trend found throughout these studies is that the strength of the whiskers increases with decreasing diameter [1]. The recent advent of compression tests[4, 5] on microfabricated pillar structures now makes it possible to probe the size-dependent strength of materials in a uniaxial fashion without requiring crystal growth in whisker form. The results from these elegant mechanical tests are consistent with the tenet that smaller is stronger, even for diameters larger than those of the whiskers.

To account for the high strengths of microfabricated metallic pillars, it has been proposed[10, 11] that mobile dislocations escape from the crystal at the nearby free surfaces before multiplying and interacting with other dislocations during the deformation process— thus leading to a state of dislocation starvation. Presumably, high stresses would then be expected since new dislocations would have to be nucleated for plasticity to proceed. While providing strong evidence for size effects in metals, these *ex-situ* tests[2, 4, 7, 18] do not permit a one-to-one relationship between the mechanical data and the microstructure evolution. In this study, we have performed direct-observation, *in-situ* experiments on microfabricated Ni pillars by utilizing a unique instrument that enables quantitative nanoscale compression tests inside a transmission electron microscope

(TEM). In addition, this technique allows us to examine potential factors such as the surface oxide[19] , pillar "sink-in"[6] , and the initial microstructure.

Single-crystal Ni pillars between 150 and 400 nm in diameter were micromachined using an FEI 235 Dual Beam focused ion beam (FIB) (for more sample preparation details see online supporting materials). TEM observations showed that the pillars had a high density of defects after FIB processing (Fig.1 A), and that these defects could be classified into two types: small, loop-like defects and long line defects often extending across the pillar. Presumably, the former are dislocation loops resulting from the ion beam irradiation and the latter are preexisting dislocations in the bulk single-crystal Ni. Counting both types of defects, the starting dislocation density of the pillars was $\sim 10^{15}/m^2$.

In-situ compression tests involving a diamond flat punch were performed on pillars of several different sizes. These tests were executed either under loading rate control (LRC, μN per second) or displacement rate control (DRC, nm per second), the details of which can be found in the online supporting materials. Remarkably, the dislocation density always decreased dramatically during the deformation test and in some cases a dislocation-free pillar was the end result. One typical example of this phenomenon, which we denote as "mechanical annealing", is shown in Fig. 1, which illustrates two consecutive compression tests run on the same pillar under LRC. The starting pillar geometry is ~150 nm in diameter at the free end, ~850 nm in length, and had a sidewall taper angle of $\sim 4.5^{o}$. Figure 1A shows the starting microstructure and Fig. 1B shows the force vs. displacement curve of the first test. After the initial test, the main section of the pillar was left completely dislocation-free (Fig 1C). Examination of the

recorded video (for videos see online supporting materials) revealed that the pillar yielded immediately upon contact with the punch. During the initial portion of the test the preexisting dislocations progressively left the pillar and were accompanied by intermittent bursts of new dislocations which correspondingly caused the load to fluctuate (Fig. 1B). The sharp increase in load starting at ~170 nm (Fig. 1B) coincided with predominantly elastic behavior. Post-test, dark-field observation under multiple two-beam conditions confirmed that this test left behind a dislocation-free pillar (Fig. 1C).

The dramatic decrease in dislocation density during the nanocompression test provides direct experimental support for the dislocation starvation mechanism that has been hypothesized based on experiments[10, 11] and simulations[17, 20]. Neither the surface oxide layer[19] nor the FIB damage layer[21] trapped dislocations inside the pillar during deformation. Presumably, the driving force for the escape of dislocations within the pillars is a combination of the applied stress and the image forces from the surface[22]. The former will activate or nucleate dislocations and the latter will assist the dislocations in moving towards the free surfaces of the crystal.

The extent to which both preexisting and newly generated dislocations ran out of the pillar was unexpected, and presented an opportunity to examine the strength of a dislocation-free pillar. Figure 1D shows the force-displacement curve of the second test on the same pillar. The mechanical response was predominantly elastic for the initial ~20 nm. Discrete plasticity then occurred, evidenced by a series of discontinuities in the curve. After the compressive displacement reached ~140nm the load steadily decreased over the next ~185 nm. The video of this test clearly showed that this steady decrease in force was due to buckling of the pillar. The load rise following this buckling (starting at

~325 nm) occurred as the punch came into contact with material at the base of the pillar (Fig. 1E).

One advantage of in situ testing is that the instantaneous contact diameter can be measured from the still frames extracted from the recorded movies (30 frames per second). This makes it possible to determine an instantaneous contact stress imposed on the pillar (force divided by the instantaneous contact area) which is more accurate than a simple engineering stress (force divided by the initial area of the top of the pillar), providing the assumption of symmetrical deformation holds true. For the test shown in Fig. 1, this assumption is reasonable, and the instantaneous stress vs. the compressive displacement for the two tests corresponding to Figs. 1B and 1D are plotted together in Fig. 1F. Interestingly, despite the approximately 15 orders of magnitude difference in starting dislocation density, the apparent yield stress achieved in both tests are quite similar. Therefore, the initial defects due to FIB processing did not significantly affect the stress response of the pillar. This suggests that the deformation of the pillar is controlled instead by the nucleation of dislocations and their propagation through the pillar. The low impact of initial microstructure on the stress-strain curve most likely is related to the fact that defects created by ion beams typically do not extend much beyond the penetration depth of the ions, which for 30keV Ga^+ in Ni is only 10-20 nm even for large incident angles[23].

However, due to the tapered geometry of the microfabricated pillars, the stress throughout the pillars is not homogeneous and the simple analysis used for calculating the instantaneous stress does not fully capture the complexity of the situation. A recent computational study has reported that a taper angle to the sidewalls of microfabricated

pillar structures can result in an overestimation of the elastic modulus and the apparent yield stress during a microcompression test[24]. Given that the microfabricated pillar shown in Fig. 1 had a side-wall taper angle of ~4.5^{o}, it is expected that the top of the pillar experienced a larger imposed stress during compression, which might result in inhomogeneous plastic deformation localized at the top of the pillar. This is in fact what happened and Fig. 1C shows a remnant of this localized deformation at the top of the pillar. In addition, the taper angle has decreased almost to zero after the initial test, consistent with there being greater deformation in regions of higher stress.

Clear evidence of inhomogeneous deformation in a second pillar, with an initial geometry of ~150 nm in free-end diameter, ~800 nm in length, and ~4.5^{o} in sidewall taper angle, is shown in Figs. 2A and 2B. In this case, a change in diameter was not detected below ~360 nm from the original free end of the pillar (below the red line in Figs. 2A and 2B) even after ~130 nm of compressive displacement. Yet, as Fig. 2B shows, the pre-existing dislocations below this point were driven out of the pillar and the entire length of the pillar was left almost dislocation-free. Thus, a tapered geometry in the investigated size regime makes it necessary to determine local stresses and strains to fully quantify the observed deformation behavior.

In order to graphically illustrate how the presence of a taper can lead to localized deformation, a purely geometric relationship describing the normalized initial stress distribution (i.e., the stress distribution in the limit of infinitesimally small strain divided by the initial stress at the free end) for pillars with different diameters and a fixed taper angle of 4.5^{o} is plotted in Fig. 2C in terms of the axial distance from the free-end surface. For a set of pillars having a fixed taper angle and a constant aspect ratio (length divided

by a consistent measure of diameter such as the free-end diameter), the ratio of the initial stress at the free end to that at the base would be independent of diameter on account of geometric self-similarity. Although the fabrication method used in this study yielded a set of pillars having a fixed taper angle, the aspect ratio varied from 1:3 to 1:5 and this variation was dictated primarily by differences in diameter than in length. As can be seen in Fig. 2C, the decay in initial stress with increasing axial distance from the free-end surface becomes more dramatic as the diameter decreases. Therefore, a set of pillars having a fixed taper angle and a constant length should exhibit increasingly more localized deformation as the diameter decreases. We found that this trend held true over the range of diameters in this study.

The extent of mechanical annealing is affected by the diameter of the pillars, and consistent with the tenet of smaller being stronger. We observed that larger diameter pillars were less likely to be dislocation-free at the end of the test. This observation is in accordance with the image forces contributing to the annihilation of dislocations at the surface, since this effect would decrease with an increase in sample dimension[22]. Figure 3 provides results from a larger pillar. In this case, a pillar ~290 nm in diameter at its free end, ~1 μm in length, and with a taper angle of ~4.5º (Fig. 3A) was compressed under DRC. Comparison of the pillar before (Fig. 3A) and after (Fig. 3B) the test revealed that most of the dislocations had been driven out of the pillar, but not as completely as in the previous examples concerning smaller diameter pillars (Figs. 1C and Fig. 2C). Figure 3C provides a plot of force and displacement vs. time of the test for the pillar shown in Fig. 3A. Arrows superimposed on the plot mark six succinctly chosen points of the data. The extremely irregular appearance of the curve is due to the discrete nature of dislocation

nucleation and motion[25]. The corresponding instantaneous stress vs. displacement curve is given in Fig. 3D with the same points transferred from Fig. 3C. Figures 3E through 3J show the microstructure at each of the six points. The punch contacted the pillar at point 1 and then from point 2 to point 3 a serrated load/stress plateau was measured. The video of this test revealed that the deformation of the pillar during the serrated plateau was the result of the activation of a single {111} slip system which can be seen clearly in the video as the crystal shearing against itself. The source indicated in Fig. 3F became exhausted at point 3 (corresponding to Fig. 3G). Between points 3 and 4 the stress built up to reach a high value of 2.6 GPa, even though the pillar still possessed a high dislocation density (Fig. 3H). This is consistent with our recent *in-situ* nanoindentation study on submicron Al grains, which demonstrated that high stresses can be achieved even in metallic grains possessing a high dislocation density [26]. At point 4 in Fig. 3C, the column again yielded but this time in a manner corresponding both to plasticity within the pillar itself and movement of the pillar as a whole into its substrate (by more than 20 nm). Many trace lines not present before this yield event (Fig. 3H) appeared along the $[2\bar{1}1]$ direction within a time interval of no more than 1/30 s (Fig. 3I). The sudden "sink-in" of the pillar into the substrate can be thought of as a hard spike punching into relatively soft ground, but in this case the "spike" and the "ground" are of the same material and the difference in hardness is purely a size effect. The sudden "sink-in" event caused the punch to lose contact with the free end of the pillar for ~1 s. The load rise after point 5 resulted from the punch re-contacting the pillar, and the subsequent load reduction leading to point 6 was the consequence of withdrawing the punch at the end of the test. Figure 3J corresponds to microstructure immediately at the end of the

experiment. The observation that a high stress (2.6 GPa) was achieved even in the presence of a high dislocation density is consistent with the theory that dislocation source starvation is the critical factor in determining strength at these small scales.

Traditionally, strain hardening is associated with strong interactions between dislocations and an increase in dislocation density throughout an experiment. In our case, however, the increases in stress levels (ignoring the fluctuations) occur more in a stepwise fashion than continuous and can be ascribed to the progressive exhaustion of dislocation sources, as is dramatically seen in Fig. 3. The underlying physical mechanism can be understood in terms of a competition between the dislocation nucleation/activation rate and the (mobile) dislocation annihilation rate. If there are enough mobile dislocations or a productive enough dislocation source to accommodate the imposed deformation a stress/load drop will occur. However, if there are not enough active sources or dislocations to accommodate the imposed deformation the stress/load will increase. Considering the large difference in stiffness between diamond (the punch material) and nickel as well as the inevitable roughness on the contact surfaces, the contact interface will serve to generate easy dislocation sources at the initial deformation stage, and this was observed in all of our experiments. However, eventually these sources become exhausted and a hardening response (stress level increase) is seen during the compression test (e.g. Fig. 1F and Fig. 3D).

Our *in-situ*, quantitative nanoscale compression tests have demonstrated that high resolution mechanical data can be directly correlated with dynamic microstructure evolution in submicron-diameter pillars. The extent to which the pillars were found to anneal through mechanical deformation was surprising. This led to the possibility of

studying dislocation-free volumes and also gave rise to atypical strain hardening where deformation was controlled by the progressive activation and subsequent exhaustion of dislocation sources. The observation that the dislocation density can fall to zero and that deformation takes place at high stresses is consistent with previous hypotheses that the strength increases in small pillar structures is controlled by the activation of new dislocation sources in a source-limited regime. In closing, this study as a whole is highly encouraging from the perspective of bridging the gap between experimentation and computational plasticity models.

References:

1. Brenner, S.S. Growth and Properties of "Whiskers". *Science* **128**, 568-575 (1958).
2. Brenner, S.S. Tensile Strength of Whiskers. *Journal of Applied Physics* **27**, 1494 (1956).
3. Herring, C. & Galt, J.K. Elastic and Plastic Properties of Very Small Metal Specimens. *Physical Review* **85**, 1060 (1952).
4. Uchic, M.D., Dimiduk, D.M., Florando, J.N. & Nix, W.D. Sample dimensions influence strength and crystal plasticity. *Science* **305**, 986-989 (2004).
5. Dimiduk, D.M., Uchic, M.D. & Parthasarathy, T.A. Size-affected single-slip behavior of pure nickel microcrystals. *Acta Mater* **53**, 4065-4077 (2005).
6. Volkert, C.A. & Lilleodden, E.T. Size effects in the deformation of sub-micron Au columns. *Philosophical Magazine* **86**, 5567-5579 (2006).
7. Greer, J.R. & Nix, W.D. Size dependence of mechanical properties of gold at the sub-micron scale. *Applied Physics a-Materials Science & Processing* **80**, 1625-1629 (2005).
8. Nix, W.D. Yielding and strain hardening of thin metal films on substrates. *Scripta Mater* **39**, 545-554 (1998).
9. Nix, W.D. Mechanical properties of thin films. *Metallurgical Transactions A* **20A**, 2217-2245 (1989).
10. Greer, J.R. & Nix, W.D. Nanoscale gold pillars strengthened through dislocation starvation. *Physical Review B* **73**, 6 (2006).

11. Nix, W.D., Greer, J.R., Feng, G. & Lilleodden, E.T. Deformation at the nanometer and micrometer length scales: Effects of strain gradients and dislocation starvation. *Thin Solid Films* **515**, 3152-3157 (2007).
12. Parthasarathy, T.A., Rao, S.I., Dimiduk, D.M., Uchic, M.D. & Trinkle, D.R. Contribution to size effect of yield strength from the stochastics of dislocation source lengths in finite samples. *Scripta Materialia* **56**, 313-316 (2007).
13. Sieradzki, K., Rinaldi, A., Friesen, C. & Peralta, P. Length scales in crystal plasticity. *Acta Mater* **54**, 4533-4538 (2006).
14. Guo, Y., Zhuang, Z., Li, X.Y. & Chen, Z. An investigation of the combined size and rate effects on the mechanical responses of FCC metals. *International Journal of Solids and Structures* **44**, 1180-1195 (2007).
15. Rabkin, E. & Srolovitz, D.J. Onset of plasticity in gold nanopillar compression. *Nano Lett* **7**, 101-107 (2007).
16. Rabkin, E., Nam, H.S. & Srolovitz, D.J. Atomistic simulation of the deformation of gold nanopillars. *Acta Mater* **55**, 2085-2099 (2007).
17. Tang, H., Schwarz, K.W. & Espinosa, H.D. Dislocation escape-related size effects in single-crystal micropillars under uniaxial compression. *Acta Mater* **55**, 1607-1616 (2007).
18. Brenner, S.S. Plastic Deformation of Copper and Silver Whiskers. *J Appl Phys* **28**, 1023 (1957).
19. Uchic, M.D., Dimiduk, D.M., Florando, J.N. & Nix, W.D. Oxide surface films on metal crystals - Response. *Science* **306**, 1134-1135 (2004).
20. Wei, Q.H. & Wu, X.L. Grain boundary dynamics under mechanical annealing in two-dimensional colloids. *Phys. Rev. E* **70**, 4 (2004).
21. Kiener, D., Motz, C., Rester, M., Jenko, M. & Dehm, G. FIB damage of Cu and possible consequences for miniaturized mechanical tests. *Materials Science and Engineering a-Structural Materials Properties Microstructure and Processing* **459**, 262-272 (2007).
22. Weertman, J. & Weertman, J.R. *Elementary dislocation theory*. (Oxford University Press, New York; 1992).
23. Ziegler, J.F., Biersach, J.P. & Littmark, U. *The Stopping and Range of Ions in Solids, Stopping and Range of Ions in Matter*, Vol. 1. (Pergamon, New York,, 1985).
24. Zhang, H., Schuster, B.E., Wei, Q. & Ramesh, K.T. The design of accurate micro-compression experiments. *Scripta Materialia* **54**, 181-186 (2006).
25. Koslowski, M. Scaling laws in plastic deformation. *Philosophical Magazine* **87**, 1175-1184 (2007).
26. Minor, A.M. *et al.* A new view of the onset of plasticity during the nanoindentation of aluminium *Nat Mater* **5**, 697-702 (2006).

Acknowledgments:

This work was supported in part by a US Department of Energy SBIR Phase II grant(DE-FG02-04ER83979) awarded to Hysitron, Inc., which does not constitute an endorsement by DOE of the views expressed in this article. This work also was supported by the Director, Office of Science, Office of Basic Energy Sciences, of the US Department of Energy under Contract No. DE-AC02-05CH11231. Chris Gilde is thanked for his assistance with video editing. Correspondence and requests for materials should be addressed to A.M.M, (aminor@lbl.gov).

Figures:

Fig. 1. Two consecutive *in situ* TEM compression tests on a FIB microfabricated 150nm-top-diameter Ni pillar with <111> orientation. (A) Dark-field (DF), TEM image of the pillar before the tests; note the high initial dislocation density. (B) Force vs. displacement curve of the first test. (C) DF TEM image of the same pillar after the first test; the pillar is now free of dislocations. (D) Force vs. displacement curve of the second test. (E) DF TEM image of the same pillar after the second test. (F) Instantaneous stress vs. compressive displacement for the two tests; the apparent yield stress is similar for both tests.

Fig. 2. Aspects of taper leading to localized deformation. (A) TEM image of a pillar before compression with a sidewall taper angle of ~4.5^{o}, a free-end diameter of ~150 nm, and a length of ~800nm. (B) TEM image of the same pillar shown in (A) after the compression test. Plastic deformation is found to concentrate on the part above the red line, which is in the same location in both images. Note that the pillar is left almost dislocation-free after the compression test, even below the red line. (C) Normalized initial stress (stress in the limit of infinitesimally small strain divided by the initial stress at the free end) vs. axial distance from the free-end surface for pillars with different diameters and a fixed taper angle of 4.5^{o}.

Fig. 3. Direct evidence of source-limited deformation: (A) Bright-field TEM image of the pillar before deformation (~290 nm free-end diameter). (B) TEM image of the same pillar after the displacement rate control test. Note the trapped dislocations. (C) Force and

displacement vs. time of the test. (D) Instantaneous stress vs. displacement of the test. (E) to (J) Frames extracted from the video that correspond to the microstructure of the pillar at the instances marked as 1 to 6 in (C) and (D), respectively.

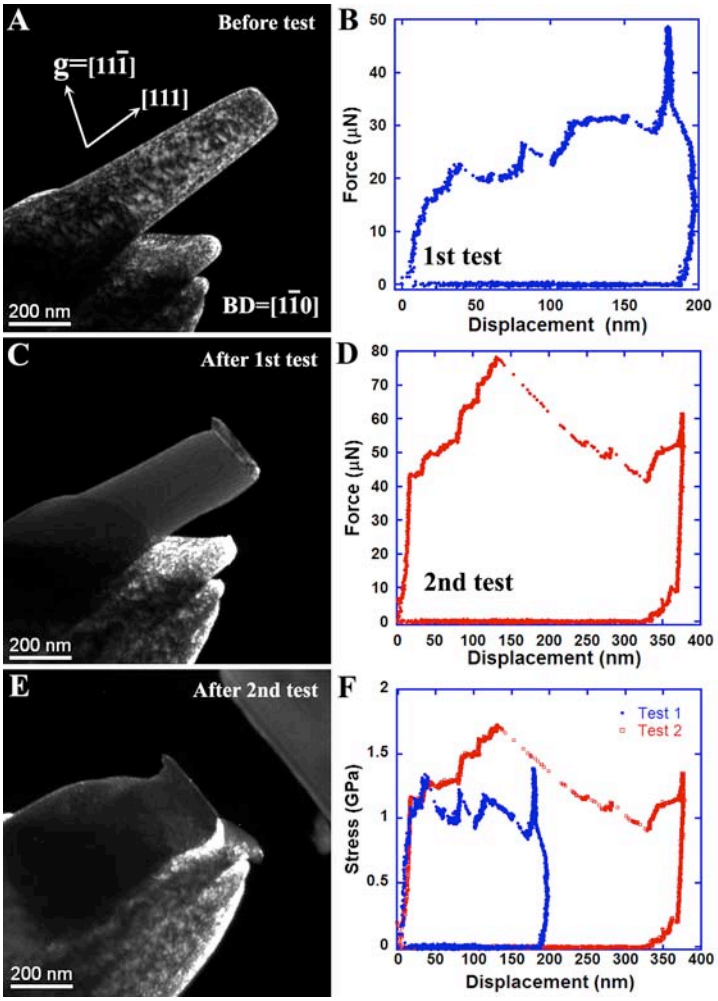

Shan et al/ Fig. 1

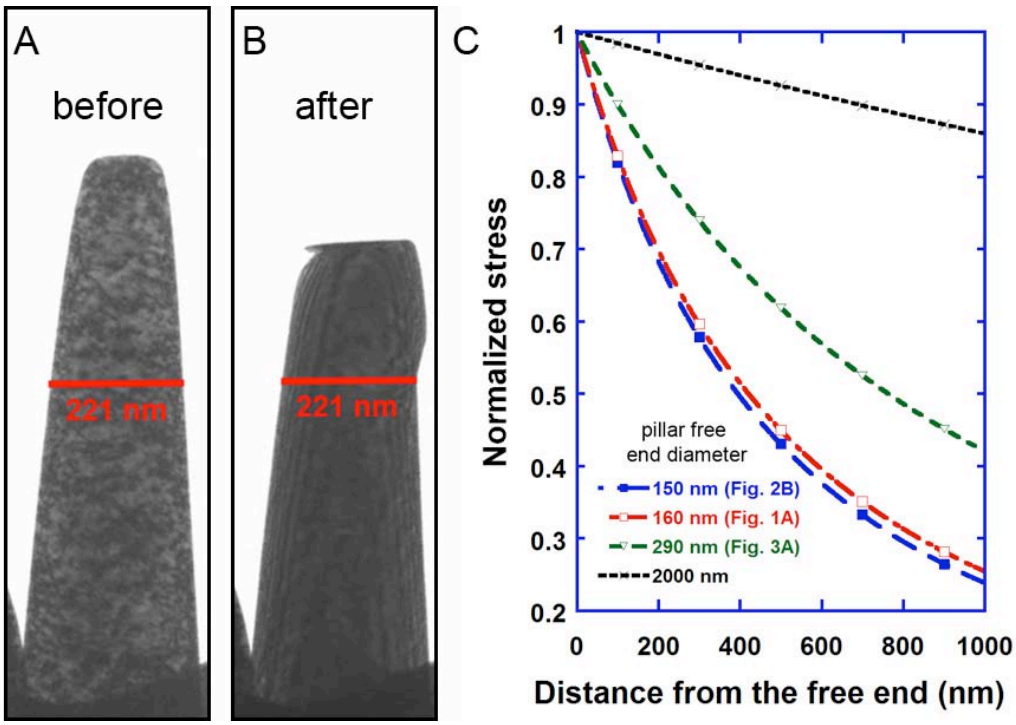

Shan et al/ Fig. 2

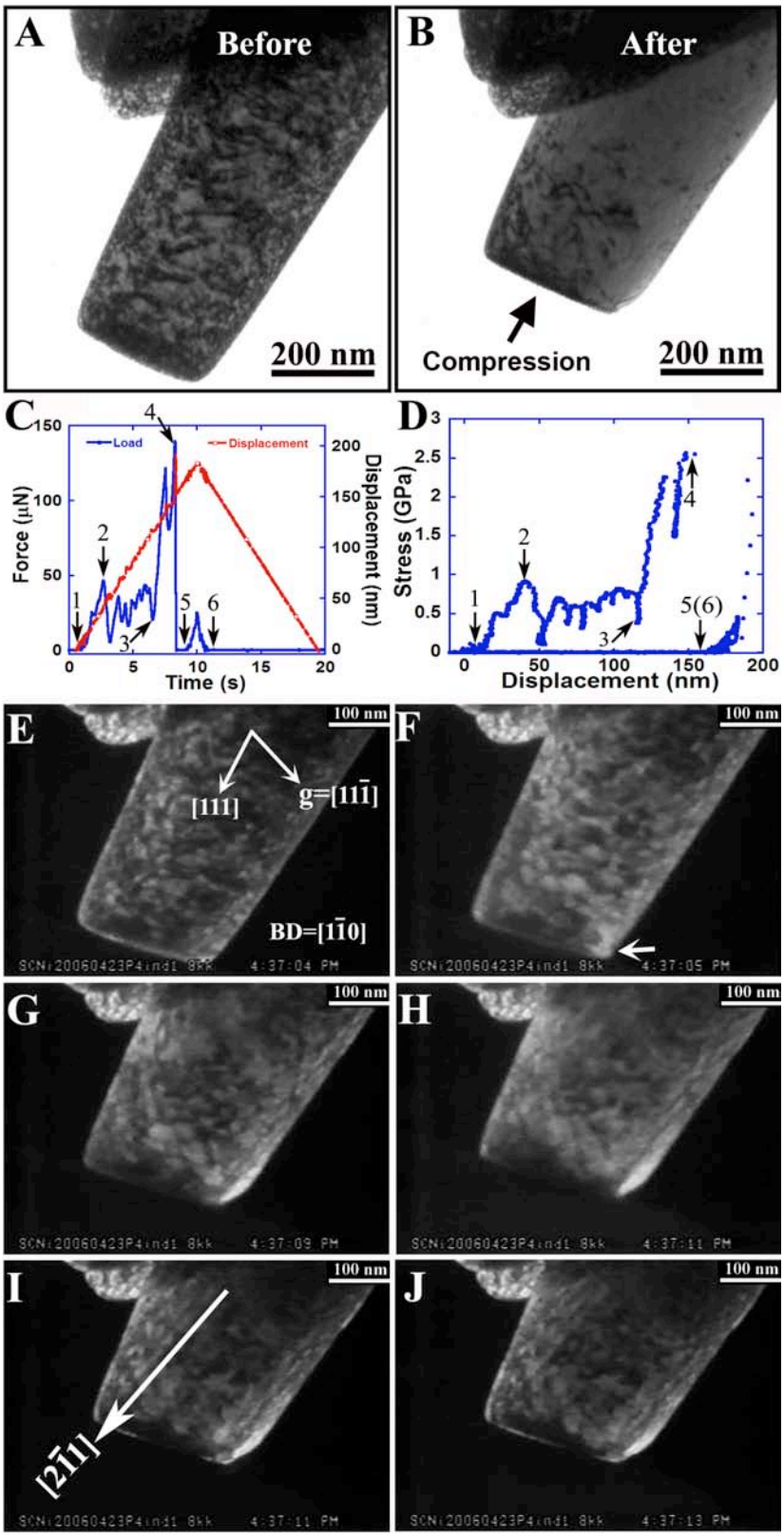

Shan et al/ Fig. 3

Mechanical Annealing and Source-limited Deformation in Submicron-diameter Ni Crystals, by Z. W. Shan *et al.*

Supporting Online Material

SOM1: Material and Sample Preparation Procedures

All of the pillars described in this manuscript were prepared from the same Ni ingot, which had a diameter of 4mm with its long axis along <110>. The purity of the material is 99.999+%. Slices of the ingot 4mm in diameter and 200 μm in thickness were fabricated with the help of spark cutting machine. These discs were then mechanically polished on both sides to a thickness of ~50 micrometer. Twin-jet polishing method was employed to thin down the sample in the middle till a perforation more than 1 mm in diameter is formed. The polishing condition is an ethanol solution containing 20% perchloric acid at ~ -15 °C. Due to the highly anisotropic nature of nickel, part of the hole edges follow clear <112> directions, with its normal along a <111> direction. The length of the <112> edges could be up to 1 mm. In order to align the sample for *in situ* TEM testing, the longest <112> polished edge was mounted to a brass substrate with crystal bond wax on a hot plate at 180°C. The <112> edge aligned to be perpendicular to the compression axis with the help of an optical microscope. The sample was then transferred to the chamber of a FEI 235 dual focused ion beam (FIB) where a flat surface was milled along the polished <112> edge, resulting in a. plateau approximately 1.5 μm ×

50 μm with a normal direction of <111>. Following this, the sample was taken out of the FIB chamber and repositioned with the normal of the platform parallel to the ion beam. Pillars with an aspect ratio ranging from 3:1 to 10:1 were machined into the surface of the platform. With the processing method depicted above, tens of pillars with precise orientation could be machined under identical conditions. During ours TEM investigations no oxide layer was observed although presumably one exists.

SOM2: Experimental Testing Methods

The *in-situ*, quantitative nanoscale compression tests were performed inside a JEOL 3010 (300kV) transmission electron microscope (TEM). Our *in-situ* TEM holder is equipped with a manual three-axis translation stage for tip-sample coarse positioning, a three-axis piezoelectric actuator for tip-sample fine positioning, and a miniature transducer providing electrostatic actuation and capacitive displacement sensing for nanomechanical testing. By running the compression tests *in situ* it enables us to build a one-to-one relationship between the quantitative mechanical data and the microstructural evolution of a deformed material at video rate resolution, i.e. 30 frames per second. The holder has a nominal force and displacement resolution of 0.1 μN and 0.5 nm, respectively.

Our control/data acquisition electronics is based on a digital signal processor and executes the mechanical testing control loop at a loop rate of 22kHz. We originally developed this instrument to carry out *in-situ*, quantitative nanoindentation; however, replacing the indenter with a flat punch enabled us to perform the pillar compression

tests. The diamond flat punch is Boron-doped and electrically connected to the body of the holder to prevent it from being charged by the electron beam.

The transducer generates a total applied load F_a proportional to V^2, where V is the applied electrostatic actuation voltage. A parallel loading configuration is employed; therefore, the contact load F_c equates to F_a-$k\delta$, where k is the effective spring constant of the spring set supporting the displaceable capacitor plate to which the punch is rigidly attached and δ is the displacement of that plate or the punch. This displacement is directly measured by a non-actuating differential capacitance detection scheme. In the case of displacement rate control, F_a is continuously adjusted by a digitally implemented proportional-integral-derivative feedback loop so that δ meets the demanded δ vs. time (t) function as closely as possible. In contrast, a predetermined F_a vs. t function is executed in the case of open-loop load rate control. The latter control mode very closely approximates true load control (i.e. control of F_c vs. t) as long as F_a overwhelmingly dominates $k\delta$.

In our pillar compression tests run under open-loop load rate control, F_a does not overwhelm $k\delta$ and thus the deviation from true load control is fairly significant and this is particularly evident whenever discrete plasticity occurs. If under true loadcontrol, a feedback loop would immediately increase F_a in response to each discrete plasticity event such that F_c continues to meet as closely as possible a demanded F_c vs. t function. However, in the case of a discrete plasticity event under open-loop load rate control, $k\delta$ suddenly increases as F_c suddenly decreases while F_a stays virtually constant over the time span of the event. But this sudden drop in contact load is nowhere to the same extent as what would have happened under displacement control. In spite of the shortcoming of

open-loop load rate control, we have chosen this control mode over true load control because feedback loop closure is not required. Feedback loop closure under true load control requires the punch contacting the pillar prior to the compression test, which might induce plastic deformation before the start of the test. Displacement rate control, on the other hand, can achieve feedback closure without the punch contacting the pillar.

SOM 3: Mechanical Data Analysis

In our manuscript, we define the stress as the instantaneous force (f_t) divided by the instantaneous contact area (S_t) between the flat diamond tip and the pillar. Although in principle it is possible to measure the contact diameter frame by frame, in practical this process become very tedious and time consuming. For the case shown in Fig. 1, it was interesting to note that sample has a well defined geometry before and after test 1. The schematic of the deformation processes is shown in Figure S1. This enables us to find the analytical solution for the relationship between the compression displacement and the contact radius.

As shown in Fig. S1, given the intial top radius as $r_{0,}$ initial bottom radius as R_0, and initial pillar height as h_0, the initial volume of the pillar can be expressed as:

$$V_0 = \frac{1}{3}\pi h_0 (R_0^{\,2} + R_0 r_0 + r_0^{\,2}) \qquad (1)$$

Assuming that the volume is conserved, for a given compression displacement d, the instant contact radius r is:

$$r = \sqrt{\frac{h_0 (R_0^{\,2} + R_0 r_0 + r_0^{\,2})}{h_0 - d} - \frac{3}{4} R_0^{\,2}} - \frac{R_0}{2} \qquad (2)$$

Using measured values for h_0, R_0 and $r_{0,}$ the relation described by equation (2) can be plotted numerically. One typical example is shown in Fig. S2, where h_0, R_0 and r_0 are taken as 850nm, 127.5 nm, 65 nm, respectively. These values are the measured values for the pillar described in Fig. S1 of the paper. From this plot the quasi-linear relationship between the contact radius and the displacement can be seen. A three-order polynomial fit can describe this relationship well, and the corresponding coefficients of the polynomial fit are shown in Fig. S2. The absolute difference (δ) between the linear fit and the three order polynomial fit is $\delta=M_2*x^2+M_3*x^3$, where M2=8.0355_10^{-5} and M3=1.4286_10^{-7} where x corresponds to compression displacement, as shown in Fig. S2. Given x=100 nm, the difference between a linear fit and the polynomial fit is δ≈1nm. This value is within the error range of our actual measurements, and thus it is our conclusion that a linear fit between the initial and final pillar diameter in response to the compression displacement can well describe the instantaneous contact radius.

In our data analysis, both the initial and the peak-load contact diameters were measured and a linear change of the contact radius in response to the compression displacement was used to calculate the instantaneous contact area according to the following formula:

$$r=r_0+(R_0-r_0)d/d_{max}, \qquad (3)$$

where r_0 and R_0 have the same meaning as that defined in Equation (1) and d_{max} corresponds to the compression displacement at the peak load.

However, it is worth pointing out that additional measures were taken if the deformation was obviously not homogeneous. For instance, if bending, "mushrooming", formation of large slip band or 'sink-in' occured then each analysis was taken on a case by case basis for determining the contact radius to use. For example, in the second test shown in Fig. 1 in our manuscript the deformation caused the pillar to buckle around 140nm displacement (the pillar effectively began to bend). Thus, the contact diameter was measured just prior to the bending events and used as the end contact diameter for the test, assuming a linear change from the beginning of that test. If the diamond punch lost contact with Ni pillar during the test due to a sudden 'sink-in' of the pillar into its substrate, the initial and final contact radii before and after the sudden 'sink-in' was measured from the corresponding extracted video frames and the instantaneous contact radius was calculated as if multiple independent compression tests were being performed. By applying these methods to calculate an instantaneous contact area we were able to take advantage of the *in situ* testing method to calculate more accurate stress data.

The sidewall taper angle of our pillars was defined as the angle between the sidewall and the axis of the pillar. Typically the taper angles were ~ 4 degrees in this study. Due to the rounding at the top edges of the pillar before deformation, the initial contact diameter was measured as the flat plateau at the top of the pillar. As an example, the pillar shown in Fig. 1 in our paper has a real value for h_0, R_0 and r_0 of 850nm, 127.5 nm, 65 nm, respectively. The nominal diameter was 160 nm if the rounding is not taken into account. For our calculations the real measured diameter was used.

In Figure 2, a simple geometrical analysis is described to demonstrate the effect of the taper geometry on the stress distribution throughout the pillar. The normalized stress

of a given plane ($\sigma_{plane}/\sigma_{top}$) can be directly related to the top diameter (d_{top}), length of the pillar (L) and taper angle (Θ) through the following formula:

$$(\sigma_{plane}/\sigma_{top})=(d_{top}/(d_{top}+2L\tan \Theta))^2 \quad (4)$$

It is worth noting that even though our *in situ* studies were limited to pillars in a smaller size regime than those studied in *ex situ* microcompression tests, the measured stresses in our experiments follow the general trend of yield stress = 353 *(diameter) $^{-0.64}$ as developed by Dimiduk, et al. from *ex situ* studies of Ni pillars [5]. While the orientation of the Ni pillars in our study is not the same as in their study, this relation holds surprising well, given the many factors that determine plasticity at small length scales, and merits further study.

SOM4: Crystallographic Analysis

During the experiments the beam direction (zone axis) was close to <110> and the image-forming diffraction vector was $[1\,\bar{1}\,1]$ for all images presented here (all of the DF images shown in this report are taken with this condition). The dislocation-free pillar seen in Figure 1C was confirmed by tilting the sample to multiple two-beam conditions and imaged in BF and DF modes. The image in Figure 1C is a representative of these conditions. It is difficult to establish crystallographic directions for specific dislocations seen during the *in situ* tests due to the dynamic nature of the events. Typically, the highly symmetric compressive axis of <111> allowed for multiple slip systems to be activated during the experiment.

Mechanical Annealing and Source-limited Deformation in Submicron-diameter Ni Crystals, by Z. W. Shan *et al*.

Mechanical Annealing and Source-limited Deformation in Submicron-diameter Ni Crystals, by Z. W. Shan *et al*.

SOM5: Video Legend

Submitted video file name	Original file name	Corresponding figure in manuscript	Description
ShanS1.avi:	SCNi20060402P3ind1.avi	None	Initial stages of deformation in a Ni pillar at higher magnification than other videos. Shown as an example of mechanical annealing.
ShanS2.avi	SCNi20060423P2ind1.avi	Fig 1A	First compression test of the pillar shown in Figure 1, with load vs. time plotted simultaneously.
ShanS3.avi	SCNi20060423P2ind2.avi	Fig 1C	Second compression test of the pillar shown in Figure 1, with load vs. time plotted simultaneously.
ShanS4.avi:	SCNi20060423P4ind1.avi	Fig 3	Compression test of the pillar shown in Figure 3 under displacement rate control with load vs. time plotted simultaneously.

Mechanical Annealing and Source-limited Deformation in Submicron-diameter Ni Crystals, by Z. W. Shan *et al*.

Figure Captions

Fig. S1. Schematic of the dynamic deformation process in the Ni pillars
Fig. S2 Compression displacement vs. instant contact radius calculated with equation 2 for a starting radius of 65nm

Figures

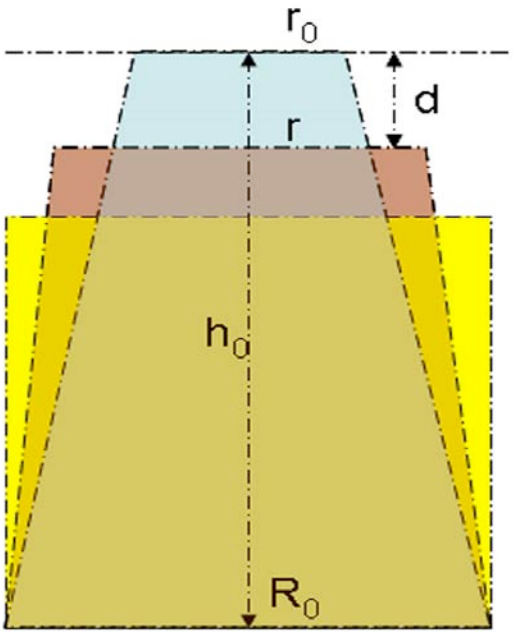

Figure S1/ Z. W. Shan et al

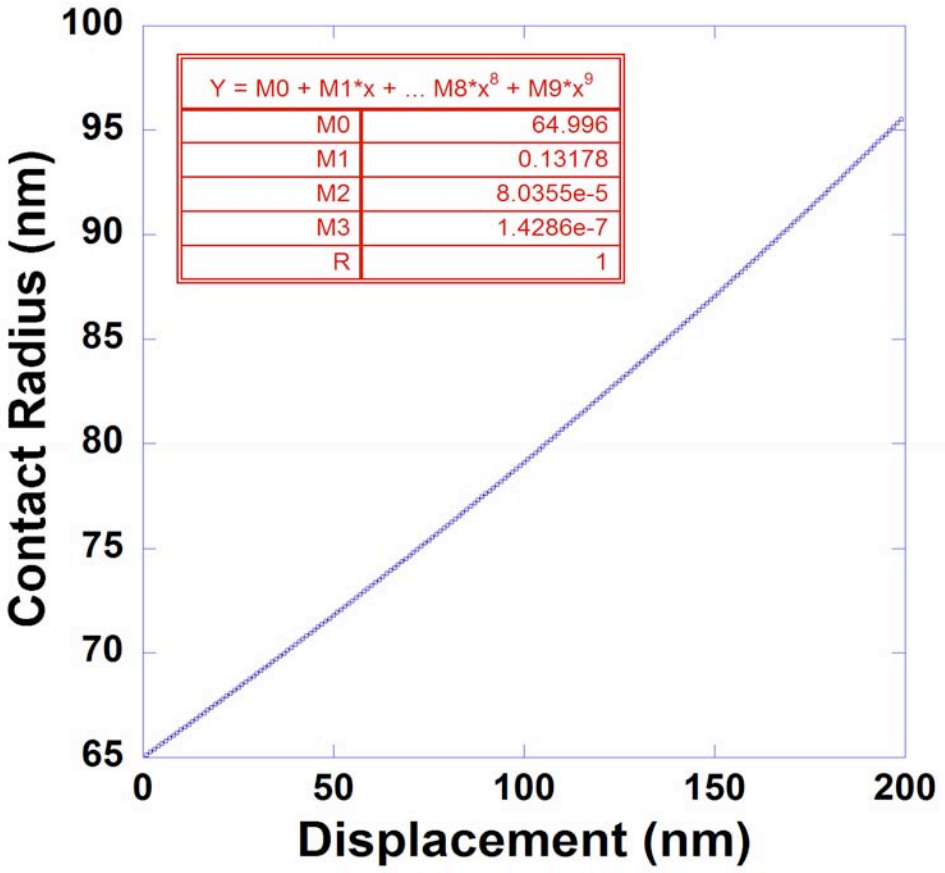

Figure S2/ Z. W. Shan et al

References:

1. Brenner, S.S. Growth and Properties of "Whiskers". *Science* **128**, 568-575 (1958).
2. Brenner, S.S. Tensile Strength of Whiskers. *Journal of Applied Physics* **27**, 1494 (1956).
3. Herring, C. & Galt, J.K. Elastic and Plastic Properties of Very Small Metal Specimens. *Physical Review* **85**, 1060 (1952).
4. Uchic, M.D., Dimiduk, D.M., Florando, J.N. & Nix, W.D. Sample dimensions influence strength and crystal plasticity. *Science* **305**, 986-989 (2004).
5. Dimiduk, D.M., Uchic, M.D. & Parthasarathy, T.A. Size-affected single-slip behavior of pure nickel microcrystals. *Acta Mater* **53**, 4065-4077 (2005).
6. Volkert, C.A. & Lilleodden, E.T. Size effects in the deformation of sub-micron Au columns. *Philosophical Magazine* **86**, 5567-5579 (2006).
7. Greer, J.R. & Nix, W.D. Size dependence of mechanical properties of gold at the sub-micron scale. *Applied Physics a-Materials Science & Processing* **80**, 1625-1629 (2005).
8. Nix, W.D. Yielding and strain hardening of thin metal films on substrates. *Scripta Mater* **39**, 545-554 (1998).
9. Nix, W.D. Mechanical properties of thin films. *Metallurgical Transactions A* **20A**, 2217-2245 (1989).
10. Greer, J.R. & Nix, W.D. Nanoscale gold pillars strengthened through dislocation starvation. *Physical Review B* **73**, 6 (2006).
11. Nix, W.D., Greer, J.R., Feng, G. & Lilleodden, E.T. Deformation at the nanometer and micrometer length scales: Effects of strain gradients and dislocation starvation. *Thin Solid Films* **515**, 3152-3157 (2007).
12. Parthasarathy, T.A., Rao, S.I., Dimiduk, D.M., Uchic, M.D. & Trinkle, D.R. Contribution to size effect of yield strength from the stochastics of dislocation source lengths in finite samples. *Scripta Materialia* **56**, 313-316 (2007).
13. Sieradzki, K., Rinaldi, A., Friesen, C. & Peralta, P. Length scales in crystal plasticity. *Acta Mater* **54**, 4533-4538 (2006).
14. Guo, Y., Zhuang, Z., Li, X.Y. & Chen, Z. An investigation of the combined size and rate effects on the mechanical responses of FCC metals. *International Journal of Solids and Structures* **44**, 1180-1195 (2007).
15. Rabkin, E. & Srolovitz, D.J. Onset of plasticity in gold nanopillar compression. *Nano Lett* **7**, 101-107 (2007).
16. Rabkin, E., Nam, H.S. & Srolovitz, D.J. Atomistic simulation of the deformation of gold nanopillars. *Acta Mater* **55**, 2085-2099 (2007).
17. Tang, H., Schwarz, K.W. & Espinosa, H.D. Dislocation escape-related size effects in single-crystal micropillars under uniaxial compression. *Acta Mater* **55**, 1607-1616 (2007).
18. Brenner, S.S. Plastic Deformation of Copper and Silver Whiskers. *J Appl Phys* **28**, 1023 (1957).
19. Uchic, M.D., Dimiduk, D.M., Florando, J.N. & Nix, W.D. Oxide surface films on metal crystals - Response. *Science* **306**, 1134-1135 (2004).

20. Wei, Q.H. & Wu, X.L. Grain boundary dynamics under mechanical annealing in two-dimensional colloids. *Phys. Rev. E* **70**, 4 (2004).
21. Kiener, D., Motz, C., Rester, M., Jenko, M. & Dehm, G. FIB damage of Cu and possible consequences for miniaturized mechanical tests. *Materials Science and Engineering a-Structural Materials Properties Microstructure and Processing* **459**, 262-272 (2007).
22. Weertman, J. & Weertman, J.R. *Elementary dislocation theory.* (Oxford University Press, New York; 1992).
23. Ziegler, J.F., Biersach, J.P. & Littmark, U. *The Stopping and Range of Ions in Solids, Stopping and Range of Ions in Matter*, Vol. 1. (Pergamon, New York,, 1985).
24. Zhang, H., Schuster, B.E., Wei, Q. & Ramesh, K.T. The design of accurate micro-compression experiments. *Scripta Materialia* **54**, 181-186 (2006).
25. Koslowski, M. Scaling laws in plastic deformation. *Philosophical Magazine* **87**, 1175-1184 (2007).
26. Minor, A.M. *et al.* A new view of the onset of plasticity during the nanoindentation of aluminium *Nat Mater* **5**, 697-702 (2006).